Nano Research
2024, 17(9): 8627–8637

ISSN 1998-0124 CN 11-5974/O4
https://doi.org/10.1007/s12274-024-6655-9

Research Article

Theoretical and experimental investigations on single-atom catalysis: Pt_1/FeO_x for water–gas shift reaction

Shan-Fei Wang[1,§], Yangyang Li[2,3,§], Haiyan Wang[1], Jin-Xia Liang[1] (✉), Chun Zhu[1] (✉), and Botao Qiao[2] (✉)

[1] *School of Chemistry and Chemical Engineering, Guizhou University, Guiyang 550025, China*
[2] *CAS Key Laboratory of Science and Technology on Applied Catalysis, Dalian Institute of Chemical Physics, Chinese Academy of Sciences, Dalian 116023, China*
[3] *University of Chinese Academy of Sciences, Beijing 100049, China*
[§] *Shan-Fei Wang and Yangyang Li contributed equally to this work.*

Received: 13 February 2024 / **Revised:** 10 March 2024 / **Accepted:** 24 March 2024

ABSTRACT

Oxide-supported metal single-atom catalysts (SACs) have exhibited excellent catalytic performance for water–gas shift (WGS) reaction. Here, we report the single-atom catalyst Pt_1/FeO_x exhibits excellent medium temperature catalytic performance for WGS reactions by the density functional theory (DFT) calculations and experimental results. The calculations indicate that H_2O molecules are easily dissociated at oxygen vacancies, and the formed *OH and *O are adsorbed on Pt_1 single atoms and the adjacent O atoms, respectively. After studying four possible reaction mechanisms, it is found that the optimal WGS reaction pathway is proceeded along the carboxyl mechanism (pathway III), in which the formation of *COOH intermediates can promote the stability of Pt_1/FeO_x SAC and the easier occurrence of WGS reaction. The energy barrier of the rate-determining step during the entire reaction cycle is only 1.16 eV, showing the high activity for the medium temperature WGS reaction on Pt_1/FeO_x SAC, which was verified by experimental results. Moreover, the calculated turnover frequencies (TOFs) of CO_2 and H_2 formation on Pt_1/FeO_x at 610 K (337 °C) can reach up to 1.14×10^{-3} s^{-1}·$site^{-1}$ through carboxyl mechanism. In this work, we further expand the application potential of Pt_1/FeO_x SAC in WGS reaction.

KEYWORDS

water–gas shift (WGS) reaction, single-atom catalyst (SAC), density functional theory (DFT), thermocatalysis

1 Introduction

With the development of economic globalization, excessive dependence on fossil fuels has led to serious energy crises and environmental issues [1]. Hydrogen energy, as one of the most promising clean energy sources, has attracted more attention due to its characteristics of cleanliness, efficiency, safety, and sustainability [2–4]. As is well known, water–gas shift (WGS) reaction ($CO + H_2O \rightleftharpoons CO_2 + H_2$) [5], as an important industrial reaction for hydrogen production and purification, which can effectively extract H_2 from water and remove CO from synthesis gas, is widely used in the ammonia synthesis, chemicals production, and fuel cell preparation [6–12]. Ma et al. [13] prepared interface catalytic structure with high density, highly dispersed atomic-level Pt species and α-MoC, which can effectively catalyze the WGS reaction for hydrogen production in a wide temperature range of nearly from room temperature to 400 °C, breaking the limitations of traditional catalysts with narrow catalytic temperature range. Wang et al. [14] reported an efficient Ru_1/FeO_x catalyst with dual active centers, which exhibits a much higher reaction rate in WGS reactions than FeO_x-supported Ru nanoparticles and other Ru based catalysts. Moreover, even under conditions rich in CO_2 and H_2, its selectivity for WGS reaches 100%, without any methane byproduct, which is impossible for Ru nanoparticles. Zhang et al. [10] synthesized a novel layered double hydroxides (LDH)-derived copper based catalyst (LD Cu) for photo-driven WGS reaction. The hot electrons generated by the localized surface plasmon resonance (LSPR) effect of Cu nanoparticles selectively promote the dissociation of water and the generation of hydrogen, enhancing the kinetics of H_2 and CO_2 release through the carboxyl pathway. The work demonstrates for the first time that catalysts based on plasma Cu nanoparticles can effectively drive WGS reactions at very low temperatures, thus opening up a new direction for the design of low-cost photo-driven catalysts for WGS and other catalytic reactions involving water activation. However, significant challenges remain in WGS reactions, such as the inevitable occurrence of methanation and other side reactions at high reaction temperatures, relatively low energy efficiency, and catalyst stability [8, 15–17]. Therefore, studying new catalysts with high stability and activity for medium temperature catalytic WGS reactions is of great significance for industrial production processes.

In 2011, a new concept of "single-atom catalysis" was proposed for the first time based on the study of the first practical single-atom catalyst (SAC) Pt_1/FeO_x [18] with ultrastability, which demonstrates extremely high activity for both CO oxidation and preferential oxidation of CO in H_2 reaction (PROX). Compared with the supported nano-metal catalysts, SACs show higher utilization of precious metal atoms and higher catalytic activity in heterogeneous catalysis, which are widely used in the fields of

Address correspondence to Jin-Xia Liang, liangjx2009@163.com; Chun Zhu, czhu2014@163.com; Botao Qiao, bqiao@dicp.ac.cn

thermal catalytic reactions, electrocatalytic reactions, and photocatalytic reactions [6, 7, 14, 19–82], such as selective hydrogenation or oxidation [62, 63], WGS reaction [6, 7, 14, 53], CO_2 reduction [19, 20], CO oxidation [23–30], oxygen reduction reaction (ORR) [75], oxygen evolution reaction (OER) [81], hydrogen evolution reaction (HER) [82], and nitrogen reduction reaction (NRR) [21, 35]. With the in-depth understanding of the stability of metal single atoms, the interactions between metal single atoms and the supports, and their catalytic mechanisms in the SACs, the concept of single-atom catalysis has been continuously enriched and developed, and a series of new and effective SACs have been emerging, such as single-cluster catalysts (SCCs) [35, 61, 83], dynamic single-atom catalysts (DSACs) [84], dual-atom-site catalysts (DASCs) [6, 73, 85], and the SACs with strong covalent metal–support interactions (CMSI) [25, 32, 48].

Noble metal SACs loaded on reducible oxide supports, such as α-Fe_2O_3, CeO_2, and TiO_2, showed remarkable catalytic activity for WGS reaction [6, 7, 53, 74, 86, 87], originating from the easy generation of lattice oxygen vacancies [18, 88–90]. Recently, the reducible oxide-supported SAC Ir_1/FeO_x has been successfully prepared, which exhibits exceptionally high activity for WGS reaction [7]. Our group [6] has also theoretically understood its high catalytic performance for WGS reaction and proposed a new dual metal active site (DMAS) redox mechanism based on the oxygen vacancy (O_{vac}) transfer driven by the synergistic changes of Fe cation of FeO_x support and the loaded Ir_1 single atom during the processes of H_2O dissociation adsorption, H atom transfer, and CO_2 generation and desorption. Similarly, reducible oxide-supported SAC Pt_1/FeO_x also exhibits high catalytic activity for extensive reactions, such as CO oxidation [18, 26, 91], NO reduction [92], selective hydrogenation [93, 94], and methanol degradation [95] reactions. However, few studies have investigated its catalytic activity for WGS reaction and compared it with Ir_1/FeO_x SAC.

In this work, extensive calculations have been performed to investigate the catalytic performance of Pt_1/FeO_x SAC for WGS reaction by using density functional theory (DFT), where four possible WGS reaction mechanisms are considered, including the traditional redox, DMAS redox, carboxyl, and formate. The calculation demonstrates that Pt_1/FeO_x SAC has higher catalytic activity for WGS reactions than Ir_1/FeO_x SAC, which is further confirmed by our further experimental results. These results could provide solid evidence to further expand the applications of Pt_1/FeO_x SAC in WGS reaction.

2 Computational and experimental details

2.1 Computational details

Based on our previous calculated models [6], the Pt_1/FeO_x SAC was constructed by replacing Fe on O3-terminated surface of Fe_2O_3(001) with Pt single atoms, which was stabilized by three surface oxygen atoms. Then all calculations of geometric and electronic properties were performed by using the Vienna *ab initio* simulation package (VASP) [96, 97]. The generalized gradient approximation (GGA) with the Perdew–Burke–Ernzerhof (PBE) [98] exchange–correlation functional was used in the calculations. The core and valence electrons were described by using the projector augmented wave (PAW) [99] method and plane-wave basis functions with a kinetic energy cut-off of 400 eV [6, 18]. The mass–velocity and Darwin relativistic effects were included through the PAW potentials due to the relativistic effects of Pt. A vacuum distance of 12 Å in the direction perpendicular to the surface was set to eliminate the artificial interplay interaction between the adjacent units of the periodic nanomaterial. Gamma point was used to sample the surface Brillouin zone after ground-state atomic geometries were obtained by minimizing the forces on the atoms below 0.02 eV/Å, while 2 × 2 × 1 Monkhorst–Pack grid was used for the partial density of states (PDOS). Considering the strong d-electron correlation effects of Fe atoms, the calculations were carried out with the DFT + U method suggested by Liechtenstein and Dudarev et al. [100–102]. The parameters were set at Coulomb repulsion parameter U = 4 eV and Hund's coupling parameter J = 1 eV according to previous study [6]. Dimer method [103] and climbing image nudged elastic band (CI-NEB) [104, 105] were used to search the transition states by relaxing the force below 0.05 eV/Å.

The adsorption energy (E_{ads}) of an adsorbate (X) on the adsorbent Pt_1/FeO_x was defined by Eq. (1)

$$E_{ads} = E_{substrate+X} - E_{substrate} - E_X \quad (1)$$

where $E_{substrate+X}$, $E_{substrate}$, and E_X represent the total energy of the X···Pt_1/FeO_x adsorption system, Pt_1/FeO_x, and free X species, respectively. The electron density difference was defined by Eq. (2)

$$\Delta\rho = \rho_{AB} - \rho_A - \rho_B \quad (2)$$

where ρ_{AB}, ρ_A, and ρ_B are the charge densities of the whole system and its components A and B, respectively. Microkinetic simulations was carried out using the CatMAP software package [106]. The calculated details were defined in the Electronic Supplementary Material (ESM).

2.2 Experimental details

2.2.1 Chemicals

Ferric nitrate nonahydrate ($Fe(NO_3)_3{\cdot}9H_2O$) was purchased from Aladdin. Sodium carbonate (Na_2CO_3) was purchased from Guang Fu. Hydrogen hexachloroiridate(IV) hexahydrate ($H_2IrCl_6{\cdot}6H_2O$) and chloroplatinic acid hexahydrate ($H_2PtCl_6{\cdot}6H_2O$) were purchased from Energy Chemical. All reagents were analytical reagent (AR) and were used directly without further purification. Deionized water was obtained from a Clever-S30 autopure system (ZhiAng Instruments Co., Ltd.).

2.2.2 Synthesis of Pt_1/FeO_x and Ir_1/FeO_x

The iron oxide supported Pt and Ir single-atom catalysts were prepared by a coprecipitation method as reported previously [7, 18]. In detail, 0.52 mL H_2PtCl_6 solution (3.8 mg_{Pt}/mL) or 0.42 mL H_2IrCl_6 solution (4.9 mg_{Ir}/mL) was added into 25 mL $Fe(NO_3)_3{\cdot}9H_2O$ (1 mol/L) aqueous solution. Then the mixture was added dropwise into 50 mL aqueous solution of Na_2CO_3 (1 mol/L) under vigorous stirring with the final pH of the solution being controlled at approximately 8. A different precipitation temperature (50 and 80 °C) was used to guarantee a higher ratio of the H_2PtCl_6 and H_2IrCl_6 in the solution was precipitated and loaded onto the FeO_x support [7, 18]. After being stirred continuously for 4 h and aged for 2 h, the resulting precipitate was filtered and washed with pure water. The recovered solid was dried at 60 °C for 12 h and calcined at 400 °C for 5 h to afford SACs, which were denoted as Pt_1/FeO_x and Ir_1/FeO_x.

2.2.3 Characterization

The actual Ir and Pt loadings of catalysts were determined by inductively coupled plasma-optical emission spectroscopy (ICP-OES) on an ICPS-8100 instrument (Shimadzu).

Aberration-corrected high-angle annular dark field scanning transmission electron microscopy (AC-HAADF-STEM) analysis was performed on an ARM300 microscope (JEOL) operated at 300 kV. Before measurements, the samples were ultrasonically

dispersed in ethanol, and then a drop of the solution was put onto the carbon film supported by a copper grid.

2.2.4 *Evaluation of activity of water–gas shift reaction*

The catalytic activity of the SACs in water–gas shift was evaluated at ambient atmosphere by using a fixed-bed reactor (quartz tube with outer diameter of 10 mm). For the purpose of providing a more accurate comparison, the catalysts' intrinsic activity was measured in a differential mode and expressed as specific rate and turnover frequency (TOF). For each test, 50 mg catalysts were diluted by 200 mg quartz sand (80–120 mesh). Before test, the catalysts were *in situ* reduced in H_2 (10 vol.% H_2/N_2, 30 mL/min) at 300 °C. After He was purged for 30 min and temperature became stable, feed gas of 1 vol.% CO, 10 vol.% H_2O, and balance He (30 mL/min) was allowed to be introduced to the fixed-bed reactor at different flow rates, giving rise to different weight hourly space velocities (WHSVs) to control the CO conversion below 20% and guaranteeing the measurement of the intrinsic activity in the kinetic region. With the aim of being comparable to the DFT calculation results, the intrinsic activity was measured at the temperatures of 300 and 350 °C, which are close to, one is slightly higher and one is slightly lower than, the temperature used in DFT calculation. The reactor temperature was recorded with a thermocouple inserted close to the catalytic bed of the reactor. For measurements at each temperature, at least three conversion data within 60 min were averaged, and all the data's difference was smaller than 5%, suggesting the catalysts were stable in the test reaction time. Gas composition at the inlet and outlet was analyzed by online gas chromatograph (GC-2014, Shimadzu) equipped with a thermal conductivity detector (TCD), with helium used as carrier gas. CO_2 and CO were separated by a Porapak N column connected to the TCD. The CO conversion, turnover frequencies (s^{-1}), and specific reaction rate (mol/(g_{metal}·h)) were calculated as follows:

$$\text{Conversion}\ (X_{CO}) = \frac{F_{co,\,in} - F_{co,\,out}}{F_{co,\,in}} \times 100\% \quad (3)$$

$$\text{Specific rate of CO} = \frac{F_t \times X_{CO}}{\text{Weight of catalyst} \times w_{metal} \times 22.4 \times 10^3} \times 60 \quad (4)$$

$$\text{TOF} = \frac{F_t \times X_{CO}}{\text{Weight of catalyst} \times w_{metal} \times \dfrac{\text{Dispersion}}{M} \times 22.4 \times 10^3 \times 60} \quad (5)$$

where F_t represents the total flow (mL/min); w_{metal} is the metal loading (wt.%); M is the molar mass (g/mol); $F_{co,\,in}$ and $F_{co,\,out}$ represent the inlet and outlet concentration of CO, respectively.

3 Results and discussion

3.1 Adsorption of H_2O and CO

For Pt_1/FeO_x SAC [18], the surface Fe atom on the O3-terminated surface of iron oxide (FeO_x) is replaced by a single Pt atom with an O_{vac} near the Pt atom to simulate the reduced FeO_x surfaces, as shown in Fig. 1(a). The single bonds [107] of Pt–O_B (1.892 Å) and Pt–O_C (1.882 Å) are formed through the strong CMSI [32] between Pt atom and O_B and O_C atoms due to the high overlap of the 5d orbitals of Pt and the 2p orbitals of O_B and O_C near the Fermi level in the partial density of states and the enrichment of electron density on Pt–O_B and Pt–O_C bonds in the electron density difference, as shown in Figs. 1(b) and 1(c). Moreover, the oxygen vacancies, which play an important role in molecule adsorption activation, dissociation, and chemical reactions, are reducible [6, 14, 18, 25–28, 34, 92, 108]. As shown in Fig. 1(d), H_2O molecules are preferentially dissociated and adsorbed on the oxygen vacancies and the adjacent O_D atoms on the surface of Pt_1/FeO_x with the adsorption energy of −1.37 eV, resulting in the formation of the higher-oxidation-state Pt(III) single atom [25], which can effectively promote the adsorption and activation of CO molecule on it. As shown in Figs. 1(e) and 1(f), the calculated PDOS and electron density difference exhibit that there is a strong interaction between Pt 5d and C 2p after CO adsorption on Pt single atom, originating from 5σ → 5d donation interaction and 5d → 2π* back-donation interaction between the 5d orbital of Pt and the 5σ and 2π* orbitals of CO adsorbate [18, 25]. Therefore, the effective co-adsorption of CO and H_2O provides prerequisites for the WGS reaction.

3.2 WGS reaction mechanism on Pt_1/FeO_x SAC

Based on the co-adsorption of CO and H_2O on the surface of Pt_1/FeO_x SAC, we explore WGS reaction by calculating four possible (Fig. S1 in the ESM) noble metal-assisted Mars–van Krevelen (MvK) mechanisms [31, 90, 109], in which the FeO_x support provides the surface lattice oxygen to participate in the reaction, namely traditional redox [110, 111], DMAS redox [6], carboxyl [10], and formate [112]. Figures 2 and 3 and Figs. S2–S8 and Tables S1–S3 in the ESM display the calculated energy profiles with the optimized structures and the selected bond lengths.

As seen from Fig. 2 and Fig. S2 in the ESM, for the redox mechanism in pathway I, the adsorbed H_2O is directly dissociated on the O_{vac} and the adjacent surface O_D atom to form two *OH on the surface of Pt_1/FeO_x SAC. Subsequently, CO is adsorbed on Pt_1 single atom and then attacks the O_C atom connected to Pt_1 to generate $*CO_2$ through TS1 with an energy barrier of 1.11 eV (*CO + O_C → $*CO_2$, 2–TS1–3), resulting in the generation of a new O_{vac} around Pt_1 single atom after the first CO_2 desorption. Then the *OH from H_2O dissociation is further dissociated into $*H_a$ and $*O_F$ atoms (*OH → $*H_a$ + $*O_F$), which is a characteristic of redox mechanism for WGS reaction [6, 111]. The H diffusion to the single Pt atom (4–5) in Fig. 2 corresponds to the steps of v–vii in Fig. S2 in the ESM, in which the $*H_a$ is transferred to Pt_1 single atom with a relatively high energy barrier of 1.77 eV ($*O_F$–H_a → $*O_F$ + Pt_1–$*H_a$, v–TS3–vi), and the $*H_b$ atom is easily transferred from O_D to O_F single atom with a small barrier energy of 0.28 eV ($*O_D$–H_b → $*O_{F1}$–$*H_b$, vi–TS4–vii) and then further transferred to Pt_1 through the highest energy barrier of 1.83 eV ($*O_F$–H_b → $*O_F$ + Pt_1–$*H_b$, 5–TS3^{I}–6). Subsequently, two *H on Pt_1 single atom react directly to generate $*H_2$ ($*H_a$ + $*H_b$ → $*H_2$, 6–7) and desorb from the surface of Pt_1/FeO_x SAC. It is found that the second H_2O is dissociatively adsorbed on the new O_{vac} to form the intermediate ii-2 in Fig. S3 in the ESM, which can promote the Pt_1/FeO_x SAC to return to its original state. Similar to the WGS reaction catalyzed by Ir_1/FeO_x SAC [6], it is very difficult for two protic H atoms of O_D–H and O_F–H to directly form H_2 on the surface of Pt_1/FeO_x SAC via the redox mechanism in pathway II (8–TS3^{II}–9) due to its energy barrier of up to 3.46 eV (Fig. 2 and Fig. S4 in the ESM). Furthermore, the calculated Bader charges for Pt_1 single atom, the second-neighboring Fe atom (Fig. 1), the C atom of absorbates, and two H atoms from H_2 of the structures in pathway I for the whole WGS reaction (Fig. S2 in the ESM) are collected in Fig. S5 in the ESM. It is obvious that the Bader charge of the second-neighboring Fe atom changes in the co-adsorption of H_2O and CO on Pt_1 single atom from the step i → iii through the bridge of Fe^{3+}–O···Pt^{2+}–O_{vac}, then in the process of the generation and desorption of the CO_2 molecule (iii → v), and subsequently in the process of both the remaining two H atoms migrating to Pt_1 single atom (v → viii). These results indicate that the active site in the redox mechanism of pathway I is delocalized around Fe and Pt_1 of Fe^{3+}–O···Pt^{2+}–O_{vac}, and thus DMAS redox mechanism [6] at Pt_1

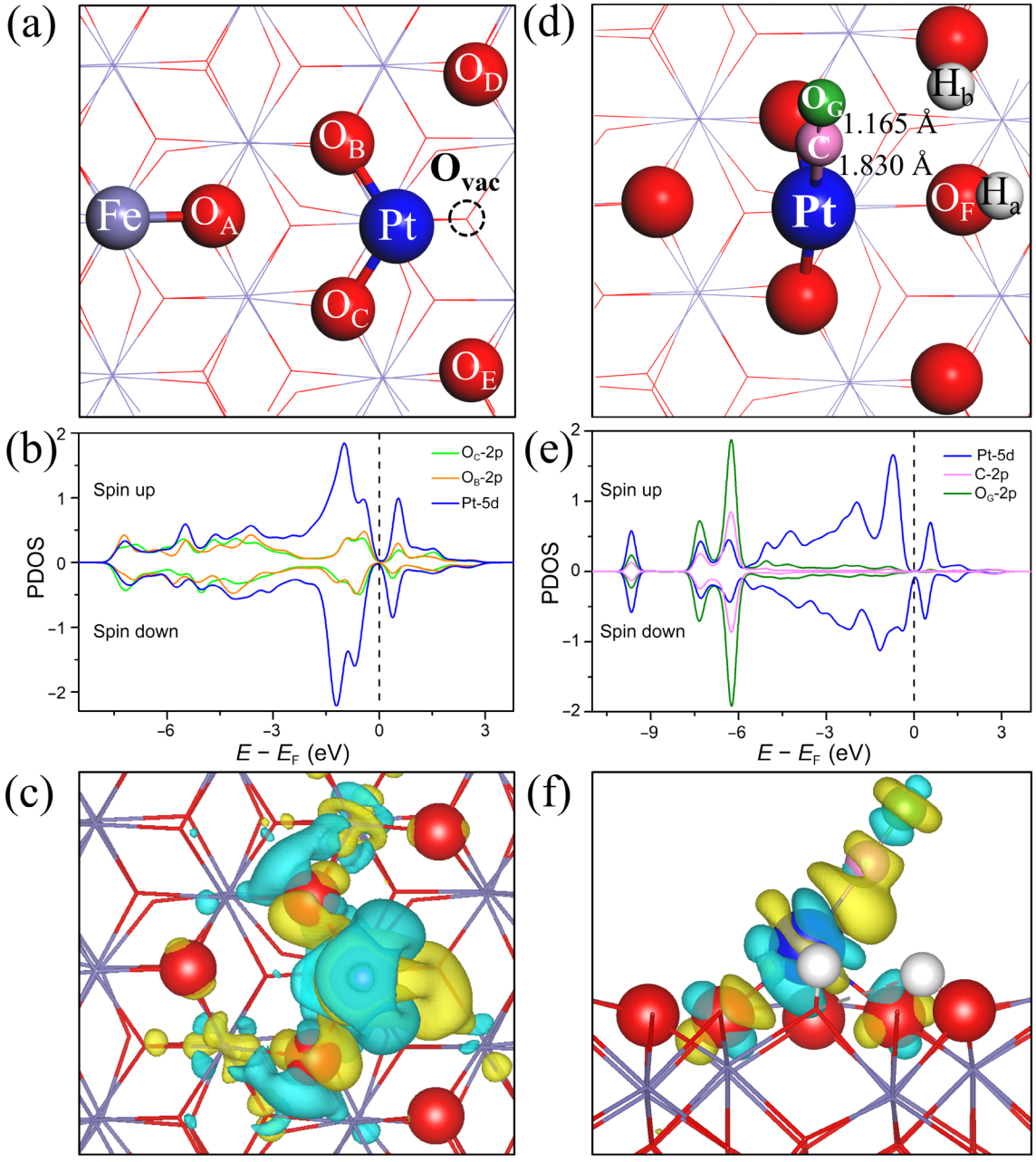

Figure 1 The local atomic arrangement of the geometric models ((a) and (d)), the PDOS ((b) and (e)), and the electron density difference ((c) and (f)) of Pt_1/FeO_x and Pt_1/FeO_x with CO and H_2O adsorption, respectively (isovalue = 0.004 a.u.). The O_A, O_B, O_C, O_D, and O_E represent the surface lattice O atoms of the support. O_F is from H_2O dissociation, and O_{vac} is located at the right side of the Pt atom. The red surface O atoms are around Pt atom. The O (dark green) and C (pink) are from CO. H atom (white), Pt atom (blue), and Fe atom (purple) are depicted.

and Fe was clearly demonstrated in the Pt_1/FeO_x SAC in redox pathway I for WGS reaction.

Carboxyl mechanism of WGS reaction over Pt_1/FeO_x SAC differs from redox mechanism, which involves the formation of carboxyl species (*COOH) [10]. As seen from Fig. 3 and and Fig. S6 in the ESM, based on the co-adsorption of CO and H_2O, the WGS reaction in pathway III undergoes the following steps. The *OH anchored on O_{vac} easily migrates to Pt_1 single atom by climbing over two small energy barriers of 0.41 and 0.33 eV. Then the *cis*-*COOH intermediate is formed by the reaction of *CO and *OH on the Pt_1 single atom with a relatively low energy barrier of 0.63 eV (*CO + *OH → *cis*-*COOH), followed by the transfer of H_b from O_D to Pt_1 single atom with the highest energy barrier of 1.16 eV (3–TS1^{III}–4). Subsequently, the *cis*-*COOH on the Pt_1 single atom rotates to *trans*-*COOH with a small energy barrier of 0.38 eV (4–TS2^{III}–5), followed by the release of CO_2 (5–TS3^{III}–6) from the surface of Pt_1/FeO_x SAC through the cleavage of the O–H bond with the energy barrier of 0.90 eV (*trans*-*COOH → CO_2 + *H). Then the remaining two *H atoms react to form H_2 (*H + *H → H_2). Compared to pathway III, pathway IV for the carboxyl mechanism undergoes a direct transformation from *cis*-*COOH to *trans*-*COOH with a very low energy barrier of 0.31 eV (3–TS1^{IV}–8), as shown in Fig. 3. However, the subsequent cleavage of the O–H bond of *trans*-*COOH, which leads to the formation of *CO_2, requires a relatively high energy barrier of 1.29 eV (8–TS2^{IV}–9), which is the rate-determining step (RDS) in pathway IV. Finally, as the *CO_2 desorbs from the surface of the catalyst with a very small energy barrier of 0.33 eV, the remaining two *H atoms overcome a relatively small energy barrier to react with each other to form H_2, which then desorbs from the surface of the catalyst, as shown in Fig. 3 and Fig. S7 in the ESM. In addition, the formate mechanism of WGS reaction on Pt_1/FeO_x SAC is also considered. However, the stable formate intermediate cannot be formed, because when *H atom gradually approaches the Pt_1 single atom, the *CO moves away from the Pt_1, as shown in Fig. S8 in the ESM.

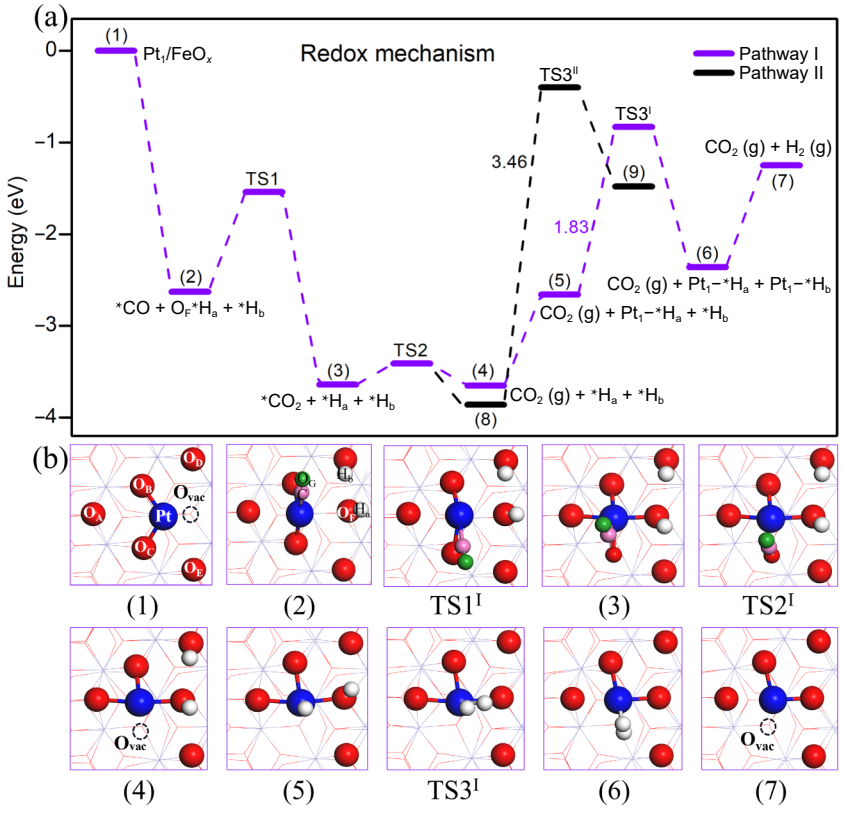

Figure 2 (a) The energy profiles of redox mechanism for WGS on the Pt_1/FeO_x catalyst in pathways I and II. (b) The corresponding optimized structures in pathway I.

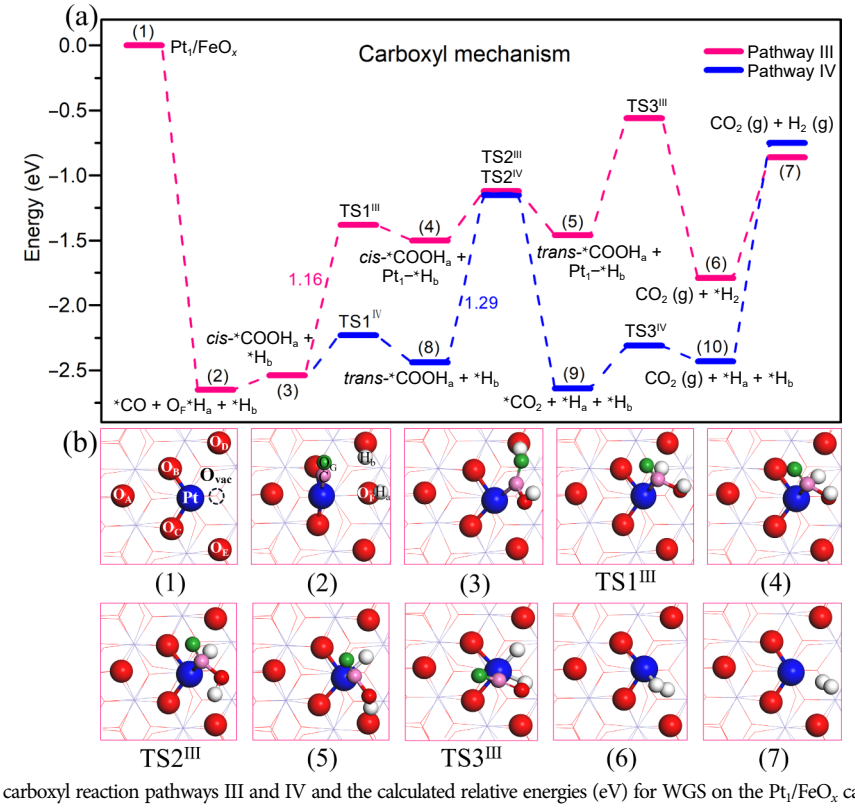

Figure 3 (a) The proposed carboxyl reaction pathways III and IV and the calculated relative energies (eV) for WGS on the Pt_1/FeO_x catalyst. (b) The corresponding optimized structures in pathway III.

Accordingly, these thermodynamic data indicate that the formation of *COOH intermediate in carboxyl reaction pathway III is favorable for WGS reaction catalyzed by Pt_1/FeO_x SAC.

3.3 Origin of WGS catalytic activities of Pt_1/FeO_x

Based on the above, it is obvious that the RDS of the optimal carboxyl reaction pathway III is the $*H_b$ atom transfer from surface O_D atom to Pt_1 single atom ($*O_D–H_b \rightarrow *O_D + Pt_1–*H_b$) with the energy barrier of 1.16 eV. Herein, to reveal the nature of high-catalytic-activity Pt_1/FeO_x SAC for WGS reaction, we analyzed the electronic properties of the related structures of intermediates vi and vii at RDS in pathway III, and the electron density difference, the Bader charge analysis, the PDOS, and the negative integrated crystal orbital Hamilton population (ICOHP)

are displayed in Fig. 4 and Table S5 in the ESM. As shown in Fig. 4(a), the electronic density is depleted in the blue areas; conversely, the density is enriched in the yellow areas. With the transfer of $*H_b$ from O_D in vi to Pt_1 single atom in vii, the electron density on $*H_b$ significantly increases, showing that more electron transfer from Pt_1 single atom to H_b in vii, which is consistent with the difference (+0.53 |e|) of the Bader charge of $*H_b$ in O_D–H_b (+0.66 |e|) and Pt_1–H_b (+0.13 |e|), as shown in Fig. 4(b). Moreover, the PDOS indicates that the interaction between the 2p of O_D and 1s of H_b in vi is stronger than that between 5d of Pt and 1s of H_b in vii, owing to the lower energy level of σ bonding of O_D–H_b than that of Pt_1–H_b, as shown in Figs. 4(c) and 4(d). The calculated ICOHP values for the bonds of O_D–H_b in vi and Pt_1–H_b in vii are −3.23 and −1.35 (Figs. 4(e) and 4(f)), respectively, which also show that O_D–H_b bond is stronger than Pt_1–H_b bond. Therefore, the transfer of $*H_b$ from O_D to Pt_1 single atom is endothermic reaction. However, for the RDS of $*O_F$–H_b → $*O_F$ + Pt_1–$*H_b$, vii → viii in the redox pathway I, the calculated Bader charge (+0.70 |e|) of H_b on O_F and the ICOHP value (−4.07) of O_F–H_b in vii (Fig. S9 in the ESM) are larger than those in the optimal carboxyl pathway III, indicating that the stronger interaction between O_F and H_b in vii leads to the higher energy barrier of 1.83 eV when the $*H_b$ atom transferred from O_F to Pt_1 single atom in the RDS of redox pathway I.

In addition, the Bader charges of Pt_1 and the second-neighboring Fe atom on the surface of Pt_1/FeO_x are complementary with the H_2O and CO co-adsorption from step i to iii (Fig. 4(b) and Fig. S6 in the ESM), showing that this process involves a DMAS [6]. However, after the migration of *OH from surface to Pt_1 single atom (iii → iv) in Fig. S6 in the ESM, the Bader charges of second-neighboring Fe atom almost unchanged (about +1.57 |e|), while the Bader charges of Pt_1 single atom is constantly changing during the next process of WGS reaction in pathway III, as shown in Fig. 4(b), indicating that the catalytic effect of Pt_1/FeO_x SAC for WGS reaction is mainly attributed to the Pt_1 single atom active center. Compared with Ir_1 of Ir_1/FeO_x, Pt_1 of Pt_1/FeO_x [6] participates in more electron transfer in the WGS reaction, thus effectively promoting its catalytic activity (Fig. S10 and Table S6 in the ESM).

3.4 Microkinetic simulations

To further evaluate the WGS reaction activity on Pt_1/FeO_x under realistic conditions, microkinetic modeling based on the reaction pathway and energies was conducted to obtain the TOFs of WGS

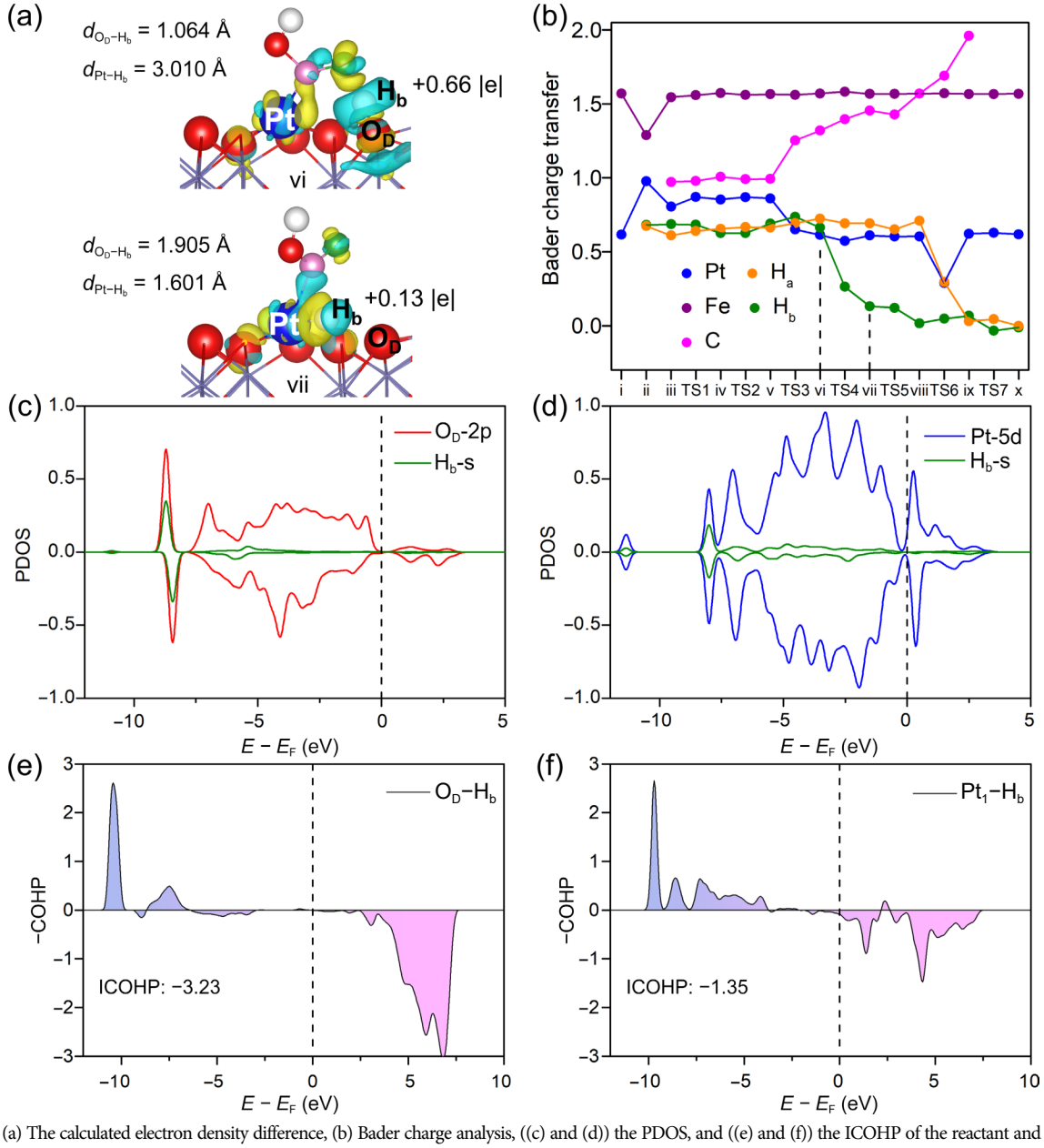

Figure 4 (a) The calculated electron density difference, (b) Bader charge analysis, ((c) and (d)) the PDOS, and ((e) and (f)) the ICOHP of the reactant and product in the RDS of vi → vii in pathway III (isovalue = 0.004 a.u.).

reaction production on Pt_1/FeO_x under the temperature range of 300–800 K and the pressure range of 1–100 bar, as shown in Fig. 5 and Table S7 in the ESM. The relevant elementary reaction steps of WGS reaction in pathways I and III are listed in Table S8 in the ESM. As seen from Fig. 5 and Table S6 in the ESM, the TOF of CO_2 and H_2 formation on Pt_1/FeO_x at 610 K (337 °C) can reach 1.14×10^{-3} s^{-1}·$site^{-1}$ in the carboxyl pathway III, comparatively close to the experimental TOF values [113, 114] of metal oxide catalysts, while the TOF of WGS reaction production at 610 K on Pt_1/FeO_x is as low as 4.04×10^{-9} s^{-1}·$site^{-1}$ in the redox pathway I, indicating that the Pt_1/FeO_x SAC has high catalytic activity for WGS reaction above 610 K (337 °C) through carboxyl mechanism. Moreover, TOF values are not affected by the pressures under the temperature range of 300–800 K due to the constant volume before and after the WGS reaction ($CO + H_2O \rightleftharpoons CO_2 + H_2$). As shown in Fig. 5(c), when the temperature is 610 K, the TOF values in pathway III approximately five orders of magnitude higher than those in pathway I. However, at a pressure of 1 bar, the TOF value gradually increases with the rise of temperature (Fig. 5(d)) especially in carboxyl pathway III, showing that the TOF values are significantly affected by temperature, and the catalytic activity of the Pt_1/FeO_x for WGS reaction is significantly improved above the medium temperature [113, 115, 116] through carboxyl mechanism.

3.5 Experimental results

3.5.1 *Characterizations of the catalysts*

The Pt_1/FeO_x and Ir_1/FeO_x catalysts were synthesized by a coprecipitation method with a normal metal loading of 0.1% to ensure the atomic dispersion. The actual loadings of the catalysts, detected by ICP-OES, were only 0.016 wt.% for Pt_1/FeO_x and 0.033 wt.% for Ir_1/FeO_x. This suggests a serious metal loss during the catalyst preparation process, consistent with our previous results [7, 18].

The high dispersion of Pt and Ir was examined by AC-HAADF-STEM. AC-HAADF-STEM images with relatively low magnification reveal clearly that neither Pt/Ir NPs nor small Pt/Ir clusters are visible (Figs. 6(a) and 6(c)), whereas high-magnification images unambiguously demonstrate the existence of single atoms of Pt and Ir dispersed on the FeO_x support (Figs. 6(b) and 6(d)).

3.5.2 *The performance of Pt_1/FeO_x and Ir_1/FeO_x catalysts*

The intrinsic activity of both Pt_1/FeO_x and Ir_1/FeO_x SACs in WGS reaction was measured at 300 and 350 °C, and the results are summarized in Table 1. It shows that at both temperatures, the Pt_1/FeO_x SAC exhibits higher intrinsic activity than Ir_1/FeO_x SAC, in good agreement with the DFT calculated results.

4 Conclusions

In this study, first-principles theoretical calculations and experiments have been performed to explore the catalytic mechanism and activity of Pt_1/FeO_x SAC for WGS reaction, where four possible reaction mechanisms, namely the redox, carboxyl, formate, and DMAS, are investigated. The results indicate that the Pt_1/FeO_x SAC has high catalytic activity for WGS reaction at medium temperature, and the most favorable pathway is the carboxyl mechanism with the transformation of *cis*-COOH to *trans*-COOH on Pt_1 single metal active center. The carboxyl intermediate is beneficial for promoting the production and desorption of CO_2 molecule with energy barrier of 1.16 eV. It is also high energy consumption (> 3.0 eV) for the direct formation of H_2 by the two protic H atoms from two different OH groups over the surface of Pt_1/FeO_x, similar to the Ir_1/FeO_x for WGS

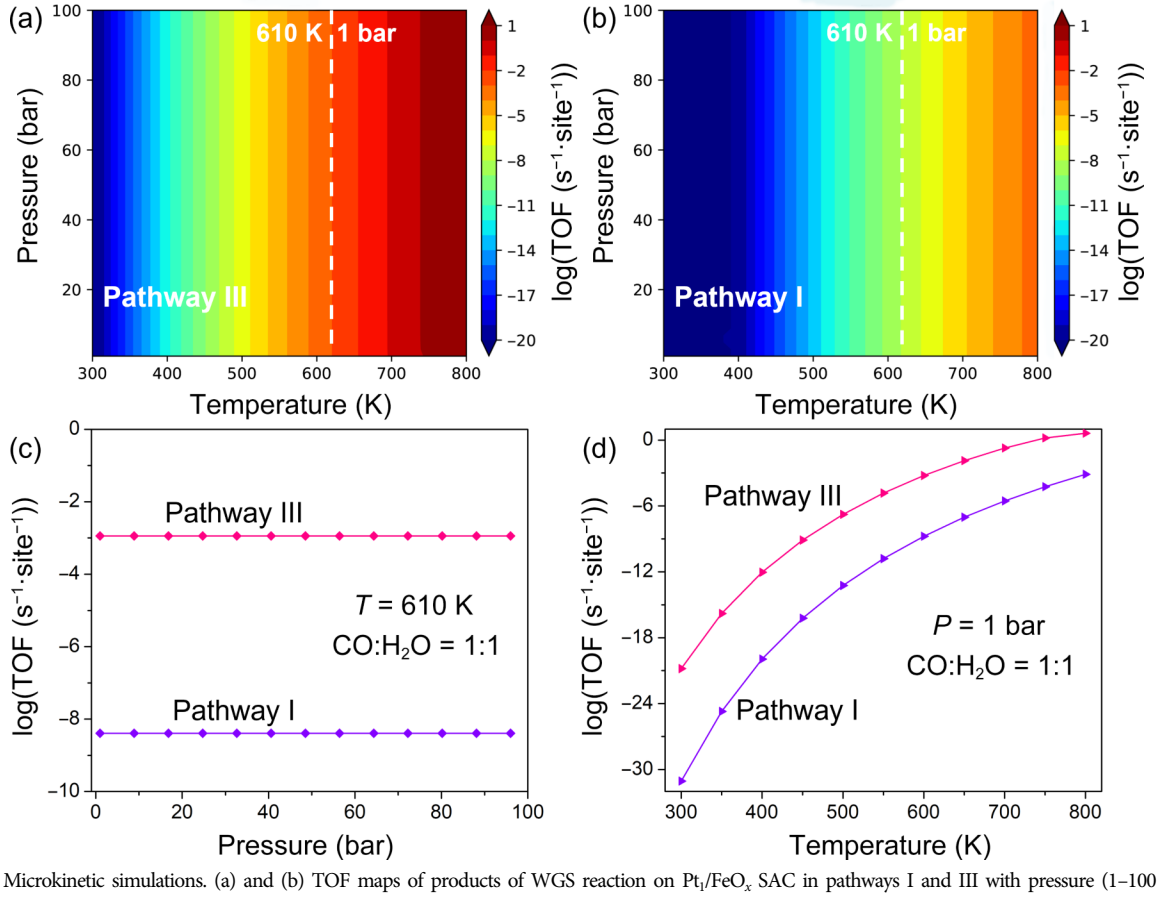

Figure 5 Microkinetic simulations. (a) and (b) TOF maps of products of WGS reaction on Pt_1/FeO_x SAC in pathways I and III with pressure (1–100 bar) and temperature (300–800 K). $CO:H_2O$ ratio is fixed at 1. (c) and (d) TOF contributions from pathway I (violet curve) and pathway III (pink curve) at the temperature of 610 K and the pressure of 1 bar, respectively.

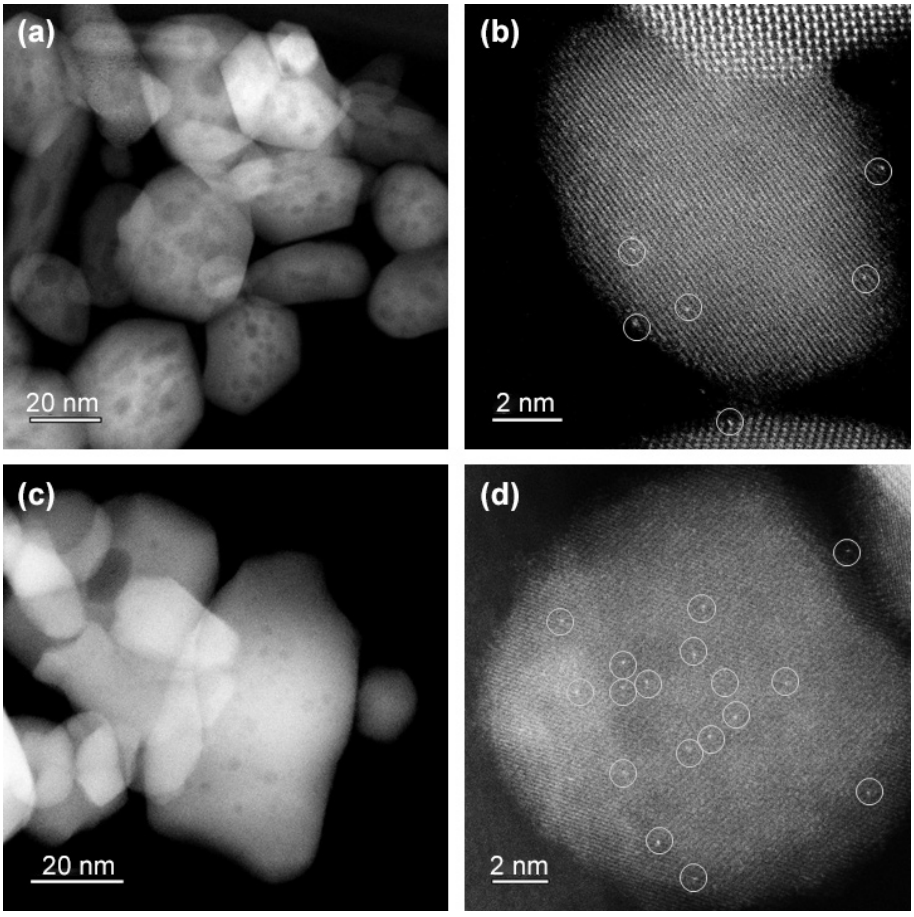

Figure 6 The AC-HAADF-STEM images of ((a) and (b)) Pt_1/FeO_x catalysts and ((c) and (d)) Ir_1/FeO_x catalysts at different magnifications. The uniformly distributed bright dots represent metal Pt and Ir single atoms.

Table 1 The intrinsic activity of Pt_1/FeO_x and Ir_1/FeO_x catalysts

Sample	Metal loading (wt.%)[a]	Con. (%)	Reaction temperature (°C)	Specific rate (mol/(g_{metal}·h))	TOF (s^{-1})
Pt_1/FeO_x	0.016	11.79	300	11.53	0.62
Ir_1/FeO_x	0.033	8.23	300	6.77	0.36
Pt_1/FeO_x	0.016	18.70	350	60.95	3.30
Ir_1/FeO_x	0.033	13.91	350	22.88	1.22

[a] The metal loadings were detected by ICP-OES.

reaction. Compared to the DMAS mechanism, the occurrence of carboxyl mechanism is almost localized at the Pt–O3 single metal active site, and the O_{vac} is not transferred between Pt_1 single atom and the adjacent Fe. The nature of high catalytic activity is the coordination ability and the local coordination environment of Pt_1 of Pt_1/FeO_x of SACs in the process of WGS reaction. Our work unearthed a new application of the first practical SAC Pt_1/FeO_x showing high catalytic activity and provides insights for understanding the catalytic nature for WGS reaction, thus facilitating rational design of new single-atom catalysts.

Acknowledgements

The authors thank the financial support from the National Natural Science Foundation of China (NSFC, Nos. 22363001 and 21963005), the NSFC Center for Single-Atom Catalysis (No. 22388102), the National Key Research and Development Program of China (No. 2022YFA1503900), and the Natural Science Special Foundation of Guizhou University (No. 202140). The calculations were performed using supercomputers at Shanghai Supercomputer Center.

Electronic Supplementary Material: Supplementary material (DFT calculated PDOS, ICOHP, other structures, and related data tables) is available in the online version of this article at https://doi.org/10.1007/s12274-024-6655-9.

References

[1] Goldthau, A. The G20 must govern the shift to low-carbon energy. *Nature* **2017**, *546*, 203–205.

[2] Dincer, I.; Aydin, M. I. New paradigms in sustainable energy systems with hydrogen. *Energy Convers. Manag.* **2023**, *283*, 116950.

[3] Blay-Roger, R.; Bach, W.; Bobadilla, L. F.; Reina, T. R.; Odriozola, J. A.; Amils, R.; Blay, V. Natural hydrogen in the energy transition: Fundamentals, promise, and enigmas. *Renew. Sust. Energy Rev.* **2024**, *189*, 113888.

[4] Zhang, C. Y.; Wang, H.; Yu, H. B.; Yi, K. X.; Zhang, W.; Yuan, X. Z.; Huang, J. H.; Deng, Y. C.; Zeng, G. M. Single-atom catalysts for hydrogen generation: Rational design, recent advances, and perspectives. *Adv. Energy Mater.* **2022**, *12*, 2200875.

[5] Yin, P.; Yang, Y. S.; Yan, H.; Wei, M. Theoretical calculations on metal catalysts toward water–gas shift reaction: A review. *Chem.—Eur. J.* **2023**, *29*, e202203781.

[6] Liang, J. X.; Lin, J.; Liu, J. Y.; Wang, X. D.; Zhang, T.; Li, J. Dual metal active sites in an Ir_1/FeO_x single-atom catalyst: A redox mechanism for the water–gas shift reaction. *Angew. Chem., Int. Ed.* **2020**, *59*, 12868–12875.

[7] Lin, J.; Wang, A. Q.; Qiao, B. T.; Liu, X. Y.; Yang, X. F.; Wang, X. D.; Liang, J. X.; Li, J.; Liu, J. Y.; Zhang, T. Remarkable performance of Ir_1/FeO_x single-atom catalyst in water gas shift reaction. *J. Am. Chem. Soc.* **2013**, *135*, 15314–15317.

[8] Chen, Y.; Lin, J.; Wang, X. D. Noble-metal based single-atom catalysts for the water–gas shift reaction. *Chem. Commun.* **2022**, *58*, 208–222.

[9] An, J. W.; Wang, G. C. Coordination-number-determined activity of copper catalyst in water–gas shift reaction. *Fuel* **2023**, *343*, 127850.

[10] Zhao, J. Q.; Bai, Y.; Li, Z. H.; Liu, J. J.; Wang, W.; Wang, P.; Yang, B.; Shi, R.; Waterhouse, G. I. N.; Wen, X. D. et al. Plasmonic Cu nanoparticles for the low-temperature photo-driven water–gas shift reaction. *Angew. Chem., Int. Ed.* **2023**, *62*, e202219299.

[11] Jin, C. C.; Wang, B. B.; Zhou, Y.; Yang, F.; Guo, P. Y.; Liu, Z.; Shen, W. J. Restructuring of the gold–carbide interface for low-temperature water–gas shift. *Chem. Commun.* **2022**, *58*, 7313–7316.

[12] Shen, H. D.; Dong, Y. J.; Yang, S. W.; He, Y.; Wang, Q. M.; Cao, Y. L.; Wang, W. B.; Wang, T. S.; Zhang, Q. Y.; Zhang, H. P. Identifying the roles of Ce^{3+}–OH and Ce–H in the reverse water–gas shift reaction over highly active Ni-doped CeO_2 catalyst. *Nano Res.* **2022**, *15*, 5831–5841.

[13] Yao, S. Y.; Zhang, X.; Zhou, W.; Gao, R.; Xu, W. Q.; Ye, Y. F.; Lin, L.; Wen, X. D.; Liu, P.; Chen, B. B. et al. Atomic-layered Au clusters on α-MoC as catalysts for the low-temperature water–gas shift reaction. *Science* **2017**, *357*, 389–393.

[14] Sun, L.; Cao, L. R.; Su, Y.; Wang, C. J.; Lin, J.; Wang, X. D. Ru_1/FeO_x single-atom catalyst with dual active sites for water gas shift reaction without methanation. *Appl. Catal. B: Environ.* **2022**, *318*, 121841.

[15] Carter, J. H.; Hutchings, G. J. Recent advances in the gold-catalysed low-temperature water–gas shift reaction. *Catalysts* **2018**, *8*, 627.

[16] Palma, V.; Ruocco, C.; Cortese, M.; Renda, S.; Meloni, E.; Festa, G.; Martino, M. Platinum based catalysts in the water gas shift reaction: Recent advances. *Metals* **2020**, *10*, 866.

[17] Yalçın, Ö.; Önal, I. DFT investigation of high temperature water gas shift reaction on chromium–iron mixed oxide catalyst. *Int. J. Hydrogen Energy* **2014**, *39*, 19563–19569.

[18] Qiao, B. T.; Wang, A. Q.; Yang, X. F.; Allard, L. F.; Jiang, Z.; Cui, Y. T.; Liu, J. Y.; Li, J.; Zhang, T. Single-atom catalysis of CO oxidation using Pt_1/FeO_x. *Nat. Chem.* **2011**, *3*, 634–641.

[19] Tian, L. C.; Hu, J. N.; Meng, Y.; Liang, J. X.; Zhu, C.; Li, J. Ultrastable nickel single-atom catalysts with high activity and selectivity for electrocatalytic CO_2 methanation. *Nano Res.* **2023**, *16*, 8987–8995.

[20] Pan, Y.; Lin, R.; Chen, Y. J.; Liu, S. J.; Zhu, W.; Cao, X.; Chen, W. X.; Wu, K. L.; Cheong, W. C.; Wang, Y. et al. Design of single-atom Co–N_5 catalytic site: A robust electrocatalyst for CO_2 reduction with nearly 100% CO selectivity and remarkable stability. *J. Am. Chem. Soc.* **2018**, *140*, 4218–4221.

[21] Hu, J. N.; Tian, L. C.; Wang, H. Y.; Meng, Y.; Liang, J. X.; Zhu, C.; Li, J. Theoretical screening of single-atom electrocatalysts of MXene-supported 3*d*-metals for efficient nitrogen reduction. *Chin. J. Catal.* **2023**, *52*, 252–262.

[22] Fang, G. Q.; Hu, J. N.; Tian, L. C.; Liang, J. X.; Lin, J.; Li, L.; Zhu, C.; Wang, X. D. Zirconium-oxo nodes of MOFs with tunable electronic properties provide effective ·OH species for enhanced methane hydroxylation. *Angew. Chem., Int. Ed.* **2022**, *61*, e202205077.

[23] Zhu, C.; Liang, J. X.; Wang, Y. G.; Li, J. Non-noble metal single-atom catalyst with MXene support: Fe_1/Ti_2CO_2 for CO oxidation. *Chin. J. Catal.* **2022**, *43*, 1830–1841.

[24] Meng, Y.; Liang, J. X.; Zhu, C.; Xu, C. Q.; Li, J. Theoretical studies of MXene-supported single-atom catalysts: Os_1/Ti_2CS_2 for low-temperature CO oxidation. *Sci. China Mater.* **2022**, *65*, 1303–1312.

[25] Liang, J. X.; Yu, Q.; Yang, X. F.; Zhang, T.; Li, J. A systematic theoretical study on FeO_x-supported single-atom catalysts: M_1/FeO_x for CO oxidation. *Nano Res.* **2018**, *11*, 1599–1611.

[26] Liang, J. X.; Yang, X. F.; Xu, C. Q.; Zhang, T.; Li, J. Catalytic activities of single-atom catalysts for CO oxidation: Pt_1/FeO_x vs. Fe_1/FeO_x. *Chin. J. Catal.* **2017**, *38*, 1566–1573.

[27] Liang, J. X.; Yang, X. F.; Wang, A. Q.; Zhang, T.; Li, J. Theoretical investigations of non-noble metal single-atom catalysis: Ni_1/FeO_x for CO oxidation. *Catal. Sci. Technol.* **2016**, *6*, 6886–6892.

[28] Liang, J. X.; Lin, J.; Yang, X. F.; Wang, A. Q.; Qiao, B. T.; Liu, J. Y.; Zhang, T.; Li, J. Theoretical and experimental investigations on single-atom catalysis: Ir_1/FeO_x for CO oxidation. *J. Phys. Chem. C* **2014**, *118*, 21945–21951.

[29] Talib, S. H.; Baskaran, S.; Yu, X. H.; Yu, Q.; Bashir, B.; Muhammad, S.; Hussain, S.; Chen, X. N.; Li, J. Non-noble metal single-atom catalyst of Co_1/MXene (Mo_2CS_2) for CO oxidation. *Sci. China Mater.* **2021**, *64*, 651–663.

[30] Chen, Y. J.; Zhuo, H. Y.; Pan, Y.; Liang, J. X.; Liu, C. G.; Li, J. Triazine COF-supported single-atom catalyst (Pd_1/trzn-COF) for CO oxidation. *Sci. China Mater.* **2021**, *64*, 1939–1951.

[31] Li, L.; Wang, A. Q.; Qiao, B. T.; Lin, J.; Huang, Y. Q.; Wang, X. D.; Zhang, T. Origin of the high activity of Au/FeO_x for low-temperature CO oxidation: Direct evidence for a redox mechanism. *J. Catal.* **2013**, *299*, 90–100.

[32] Qiao, B. T.; Liang, J. X.; Wang, A. Q.; Xu, C. Q.; Li, J.; Zhang, T.; Liu, J. J. Ultrastable single-atom gold catalysts with strong covalent metal–support interaction (CMSI). *Nano Res.* **2015**, *8*, 2913–2924.

[33] Li, J.; Li, Y. D.; Zhang, T. Recent progresses in the research of single-atom catalysts. *Sci. China Mater.* **2020**, *63*, 889–891.

[34] Tang, Y.; Wang, Y. G.; Liang, J. X.; Li, J. Investigation of water adsorption and dissociation on Au_1/CeO_2 single-atom catalysts using density functional theory. *Chin. J. Catal.* **2017**, *38*, 1558–1565.

[35] Ma, X. L.; Liu, J. C.; Xiao, H.; Li, J. Surface single-cluster catalyst for N_2-to-NH_3 thermal conversion. *J. Am. Chem. Soc.* **2018**, *140*, 46–49.

[36] Tian, L. C.; Fang, G. Q.; Zhou, Y.; Yu, W. J.; Li, L.; Hu, J. N.; Wang, H. Y.; Liang, J. X.; Zhu, C.; Wang, X. D.; Lin, J. Deciphering structural evolution of adsorbed ˙OH species on Zr-oxo nodes of UiO-66 to modulate methane hydroxylation. *J. Mater. Chem. A* **2024**, *12*, 3565–3574.

[37] Liu, J. C.; Wang, Y. G.; Li, J. Toward rational design of oxide-supported single-atom catalysts: Atomic dispersion of gold on ceria. *J. Am. Chem. Soc.* **2017**, *139*, 6190–6199.

[38] Li, J.; Stephanopoulos, M. F.; Xia, Y. N. Introduction: Heterogeneous single-atom catalysis. *Chem. Rev.* **2020**, *120*, 11699–11702.

[39] Meng, Y.; Wang, H. Y.; Liang, J. X.; Zhu, C.; Li, J. Computational screening of $Pt_1@Ti_3C_2T_2$ (T = O, S) MXene catalysts for water–gas shift reaction. *Precis. Chem.* **2024**, *2*, 70–80.

[40] Zhuo, H. Y.; Zhang, X.; Liang, J. X.; Yu, Q.; Xiao, H.; Li, J. Theoretical understandings of graphene-based metal single-atom catalysts: Stability and catalytic performance. *Chem. Rev.* **2020**, *120*, 12315–12341.

[41] Zhu, C.; Liang, J. X.; Meng, Y.; Lin, J.; Cao, Z. X. Mn-corrolazine-based 2D-nanocatalytic material with single Mn atoms for catalytic oxidation of alkane to alcohol. *Chin. J. Catal.* **2021**, *42*, 1030–1039.

[42] Wang, A. Q.; Li, J.; Zhang, T. Heterogeneous single-atom catalysis. *Nat. Rev. Chem.* **2018**, *2*, 65–81.

[43] Li, J.; Liu, J.; Zhang, T. Preface to the special issue of the international symposium on single-atom catalysis (ISSAC-2016). *Chin. J. Catal.* **2017**, *38*, 1431.

[44] Huang, Z. W.; Liang, J. X.; Tang, D. M.; Chen, Y. X.; Qu, W. Y.; Hu, X. L.; Chen, J. X.; Dong, Y. Y.; Xu, D. R.; Golberg, D. et al. Interplay between remote single-atom active sites triggers speedy catalytic oxidation. *Chem* **2022**, *8*, 3008–3017.

[45] Zhu, C.; Liang, J. X.; Cao, Z. X. Mn–O–O electron spin flip

mechanism triggered by the visible-light irradiation for the generation of an active Mn(V)-oxo complex from O_2: Insight from density functional calculations. *J. Phys. Chem. C* **2018**, *122*, 20781–20786.

[46] Wu, J.; Long, T. R.; Wang, H. Y.; Liang, J. X.; Zhu, C. Oriented external electric fields regurating the reaction mechanism of CH_4 oxidation catalyzed by Fe(IV)-oxo-corrolazine: Insight from density functional calculations. *Front. Chem.* **2022**, *10*, 896944.

[47] Long, T. R.; Wan, H. Y.; Zhang, J. Q.; Wu, J.; Liang, J. X.; Zhu, C. The high-effective catalytic degradation of benzo[a]pyrene by Mn-corrolazine regulated by oriented external electric field: Insight from DFT study. *Front. Chem.* **2022**, *10*, 884105.

[48] Lang, R.; Xi, W.; Liu, J. C.; Cui, Y. T.; Li, T. B.; Lee, A. F.; Chen, F.; Chen, Y.; Li, L.; Li, L. et al. Non defect-stabilized thermally stable single-atom catalyst. *Nat. Commun.* **2019**, *10*, 234.

[49] Liu, Y.; Liu, J. C.; Li, T. H.; Duan, Z. H.; Zhang, T. Y.; Yan, M.; Li, W. L.; Xiao, H.; Wang, Y. G.; Chang, C. R. et al. Unravelling the enigma of nonoxidative conversion of methane on iron single-atom catalysts. *Angew. Chem., Int. Ed.* **2020**, *59*, 18586–18590.

[50] Liu, J. C.; Xiao, H.; Li, J. Constructing high-loading single-atom/cluster catalysts via an electrochemical potential window strategy. *J. Am. Chem. Soc.* **2020**, *142*, 3375–3383.

[51] Liu, W. G.; Zhang, L. L.; Liu, X.; Liu, X. Y.; Yang, X. F.; Miao, S.; Wang, W. T.; Wang, A. Q.; Zhang, T. Discriminating catalytically active FeN_x species of atomically dispersed Fe–N–C catalyst for selective oxidation of the C–H bond. *J. Am. Chem. Soc.* **2017**, *139*, 10790–10798.

[52] Li, T. B.; Liu, F.; Tang, Y.; Li, L.; Miao, S.; Su, Y.; Zhang, J. Y.; Huang, J. H.; Sun, H.; Haruta, M. et al. Maximizing the number of interfacial sites in single-atom catalysts for the highly selective, solvent-free oxidation of primary alcohols. *Angew. Chem., Int. Ed.* **2018**, *57*, 7795–7799.

[53] Guan, H. L.; Lin, J.; Qiao, B. T.; Miao, S.; Wang, A. Q.; Wang, X. D.; Zhang, T. Enhanced performance of Rh_1/TiO_2 catalyst without methanation in water–gas shift reaction. *AIChE J.* **2017**, *63*, 2081–2088.

[54] Ren, Y. J.; Tang, Y.; Zhang, L. L.; Liu, X. Y.; Li, L.; Miao, S.; Su, D. S.; Wang, A. Q.; Li, J.; Zhang, T. Unraveling the coordination structure–performance relationship in Pt_1/Fe_2O_3 single-atom catalyst. *Nat. Commun.* **2019**, *10*, 4500.

[55] Pan, Y.; Chen, Y. J.; Wu, K. L.; Chen, Z.; Liu, S. J.; Cao, X.; Cheong, W. C.; Meng, T.; Luo, J.; Zheng, L. R. et al. Regulating the coordination structure of single-atom Fe-N_xC_y catalytic sites for benzene oxidation. *Nat. Commun.* **2019**, *10*, 4290.

[56] Talib, S. H.; Hussain, S.; Baskaran, S.; Lu, Z. S.; Li, J. Chromium single-atom catalyst with graphyne support: A theoretical study of NO oxidation and reduction. *ACS Catal.* **2020**, *10*, 11951–11961.

[57] Li, Z.; Chen, Y. J.; Ji, S. F.; Tang, Y.; Chen, W. X.; Li, A.; Zhao, J.; Xiong, Y.; Wu, Y. E.; Gong, Y. et al. Iridium single-atom catalyst on nitrogen-doped carbon for formic acid oxidation synthesized using a general host–guest strategy. *Nat. Chem.* **2020**, *12*, 764–772.

[58] Liu, K. P.; Tang, Y.; Yu, Z. Y.; Ge, B. H.; Ren, G. Q.; Ren, Y. J.; Su, Y.; Zhang, J. C.; Sun, X. C.; Chen, Z. Q. et al. High-loading and thermally stable $Pt_1/MgAl_{1.2}Fe_{0.8}O_4$ single-atom catalysts for high-temperature applications. *Sci. China Mater.* **2020**, *63*, 949–958.

[59] Chen, Z.; Chen, Y. J.; Chao, S. L.; Dong, X. B.; Chen, W. X.; Luo, J.; Liu, C. G.; Wang, D. S.; Chen, C.; Li, W. et al. Single-atom Au^I–N_3 site for acetylene hydrochlorination reaction. *ACS Catal.* **2020**, *10*, 1865–1870.

[60] Zhou, M. X.; Yang, M.; Yang, X. F.; Zhao, X. C.; Sun, L.; Deng, W. Q.; Wang, A. Q.; Li, J.; Zhang, T. On the mechanism of H_2 activation over single-atom catalyst: An understanding of Pt_1/WO_x in the hydrogenolysis reaction. *Chin. J. Catal.* **2020**, *41*, 524–532.

[61] Zhang, S. R.; Nguyen, L.; Liang, J. X.; Shan, J. J.; Liu, J. Y.; Frenkel, A. I.; Patlolla, A.; Huang, W. X.; Li, J.; Tao, F. Catalysis on singly dispersed bimetallic sites. *Nat. Commun.* **2015**, *6*, 7938.

[62] Xing, D. H.; Xu, C. Q.; Wang, Y. G.; Li, J. Heterogeneous single-cluster catalysts for selective semihydrogenation of acetylene with graphdiyne-supported triatomic clusters. *J. Phys. Chem. C* **2019**, *123*, 10494–10500.

[63] Zhou, D.; Zhang, L. L.; Liu, X. Y.; Qi, H. F.; Liu, Q. G.; Yang, J.; Su, Y.; Ma, J. Y.; Yin, J. Z.; Wang, A. Q. Tuning the coordination environment of single-atom catalyst M-N-C towards selective hydrogenation of functionalized nitroarenes. *Nano Res.* **2022**, *15*, 519–527.

[64] Han, B.; Lang, R.; Tang, H. L.; Xu, J.; Gu, X. K.; Qiao, B. T.; Liu, J. Y. Superior activity of Rh_1/ZnO single-atom catalyst for CO oxidation. *Chin. J. Catal.* **2019**, *40*, 1847–1853.

[65] Yang, X. F.; Wang, A. Q.; Qiao, B. T.; Li, J.; Liu, J. Y.; Zhang, T. Single-atom catalysts: A new frontier in heterogeneous catalysis. *Acc. Chem. Res.* **2013**, *46*, 1740–1748.

[66] Zhang, L. L.; Ren, Y. J.; Liu, W. G.; Wang, A. Q.; Zhang, T. Single-atom catalyst: A rising star for green synthesis of fine chemicals. *Natl. Sci. Rev.* **2018**, *5*, 653–672.

[67] Lang, R.; Du, X. R.; Huang, Y. K.; Jiang, X. Z.; Zhang, Q.; Guo, Y. L.; Liu, K. P.; Qiao, B. T.; Wang, A. Q.; Zhang, T. Single-atom catalysts based on the metal–oxide interaction. *Chem. Rev.* **2020**, *120*, 11986–12043.

[68] Yang, W. N.; Zhao, X. G.; Wang, Y.; Wang, R.; Yang, W. H.; Peng, Y.; Li, J. H. Selective dissolution to synthesize densely populated Pt single atom catalyst. *Nano Res.* **2023**, *16*, 219–227.

[69] Liu, W. G.; Zhang, L. L.; Yan, W. S.; Liu, X. Y.; Yang, X. F.; Miao, S.; Wang, W. T.; Wang, A. Q.; Zhang, T. Single-atom dispersed Co–N–C catalyst: Structure identification and performance for hydrogenative coupling of nitroarenes. *Chem. Sci.* **2016**, *7*, 5758–5764.

[70] Xu, Q.; Cheng, X. W.; Zhang, N. Q.; Tu, Y.; Wu, L. H.; Pan, H. B.; Hu, J.; Ding, H. H.; Zhu, J. F.; Li, Y. D. Unraveling the advantages of Pd/CeO_2 single-atom catalysts in the NO + CO reaction by model catalysts. *Nano Res.* **2023**, *16*, 8882–8892.

[71] Gu, X. K.; Qiao, B. T.; Huang, C. Q.; Ding, W. C.; Sun, K. J.; Zhan, E. S.; Zhang, T.; Liu, J. Y.; Li, W. X. Supported single Pt_1/Au_1 atoms for methanol steam reforming. *ACS Catal.* **2014**, *4*, 3886–3890.

[72] Lang, R.; Li, T. B.; Matsumura, D.; Miao, S.; Ren, Y. J.; Cui, Y. T.; Tan, Y.; Qiao, B. T.; Li, L.; Wang, A. Q. et al. Hydroformylation of olefins by a rhodium single-atom catalyst with activity comparable to $RhCl(PPh_3)_3$. *Angew. Chem., Int. Ed.* **2016**, *55*, 16054–16058.

[73] Zhang, Z. W.; Zhang, L.; Wang, X. Y.; Feng, Y.; Liu, X. W.; Sun, W. M. Rational design of graphyne-based dual-atom site catalysts for CO oxidation. *Nano Res.* **2023**, *16*, 343–351.

[74] Su, Y. Q.; Xia, G. J.; Qin, Y. Y.; Ding, S. J.; Wang, Y. G. Lattice oxygen self-spillover on reducible oxide supported metal cluster: The water–gas shift reaction on Cu/CeO_2 catalyst. *Chem. Sci.* **2021**, *12*, 8260–8267.

[75] Lu, Z. Y.; Wang, B.; Hu, Y. F.; Liu, W.; Zhao, Y. F.; Yang, R. O.; Li, Z. P.; Luo, J.; Chi, B.; Jiang, Z. et al. An isolated zinc–cobalt atomic pair for highly active and durable oxygen reduction. *Angew. Chem., Int. Ed.* **2019**, *58*, 2622–2626.

[76] Gan, T.; Wang, D. S. Atomically dispersed materials: Ideal catalysts in atomic era. *Nano Res.* **2024**, *17*, 18–38.

[77] Zhu, Q. T.; Shen, H. L.; Han, C.; Huang, L.; Zhou, Y. T.; Du, Y. X.; Kang, X.; Zhu, M. Z. Rationally construction of atomic-precise interfacial charge transfer channel and strong build-in electric field in nanocluster-based Z-scheme heterojunctions with enhanced photocatalytic hydrogen production. *Nano Res.* **2024**, *17*, 5002–5010.

[78] Li, R. Z.; Wang, D. S. Understanding the structure–performance relationship of active sites at atomic scale. *Nano Res.* **2022**, *15*, 6888–6923.

[79] Zheng, X. B.; Li, B. B.; Wang, Q. S.; Wang, D. S.; Li, Y. D. Emerging low-nuclearity supported metal catalysts with atomic level precision for efficient heterogeneous catalysis. *Nano Res.* **2022**, *15*, 7806–7839.

[80] Sun, J. K.; Pan, Y. W.; Xu, M. Q.; Sun, L.; Zhang, S. L.; Deng, W. Q.; Zhai, D. Heteroatom doping regulates the catalytic performance of single-atom catalyst supported on graphene for ORR. *Nano Res.* **2024**, *17*, 1086–1093.

[81] Zhou, Y. N.; Li, J.; Gao, X. P.; Chu, W.; Gao, G. P.; Wang, L. W. Recent advances in single-atom electrocatalysts supported on two-dimensional materials for the oxygen evolution reaction. *J. Mater. Chem. A* **2021**, *9*, 9979–9999.

[82] Aggarwal, P.; Sarkar, D.; Awasthi, K.; Menezes, P. W. Functional role of single-atom catalysts in electrocatalytic hydrogen evolution: Current developments and future challenges. *Coord. Chem. Rev.* **2022**, *452*, 214289.

[83] Liu, J. C.; Ma, X. L.; Li, Y.; Wang, Y. G.; Xiao, H.; Li, J. Heterogeneous Fe_3 single-cluster catalyst for ammonia synthesis via an associative mechanism. *Nat. Commun.* **2018**, *9*, 1610.

[84] Wang, Y. G.; Mei, D. H.; Glezakou, V. A.; Li, J.; Rousseau, R. Dynamic formation of single-atom catalytic active sites on ceria-supported gold nanoparticles. *Nat. Commun.* **2015**, *6*, 6511.

[85] Wang, Z. S.; Cheng, M.; Liu, Y.; Wu, Z. W.; Gu, H. Y.; Huang, Y.; Zhang, L. Z.; Liu, X. Dual-atomic-site catalysts for molecular oxygen activation in heterogeneous thermo-/electro-catalysis. *Angew. Chem., Int. Ed.* **2023**, *62*, e202301483.

[86] Wu, D. F.; Zhou, S. Y.; Du, C. C.; Li, J.; Huang, J. Y.; Shen, H. X.; Datye, A. K.; Jiang, S.; Miller, J. T.; Lin, S. et al. The proximity between hydroxyl and single atom determines the catalytic reactivity of Rh_1/CeO_2 single-atom catalysts. *Nano Res.* **2024**, *17*, 397–406.

[87] Tiwari, R.; Sarkar, B.; Tiwari, R.; Pendem, C.; Sasaki, T.; Saran, S.; Bal, R. Pt nanoparticles with tuneable size supported on nanocrystalline ceria for the low temperature water–gas-shift (WGS) reaction. *J. Mol. Catal. A: Chem.* **2014**, *395*, 117–123.

[88] Shi, Q. Q.; Wang, Y. H.; Guo, S.; Han, Z. K.; Ta, N.; Li, G.; Baiker, A. NO reduction with CO over CuO_x/CeO_2 nanocomposites: Influence of oxygen vacancies and lattice strain. *Catal. Sci. Technol.* **2021**, *11*, 6543–6552.

[89] Chen, J.; Bogdanov, N. A.; Usvyat, D.; Fang, W.; Michaelides, A.; Alavi, A. The color center singlet state of oxygen vacancies in TiO_2. *J. Chem. Phys.* **2020**, *153*, 204704.

[90] Liu, L. Q.; Zhou, F.; Wang, L. G.; Qi, X. J.; Shi, F.; Deng, Y. Q. Low-temperature CO oxidation over supported Pt, Pd catalysts: Particular role of FeO_x support for oxygen supply during reactions. *J. Catal.* **2010**, *274*, 1–10.

[91] Qiao, B.; Liu, J.; Allard, L.; Wang, A.; Cui, Y.; Zhang, T.; Yang, X.; Li, J.; Jiang, Z. Single-atom catalysis: Pt_1/FeO_x for CO oxidation and preferential oxidation of CO in H_2. *Microsc. Microanal.* **2012**, *18*, 350–351.

[92] Lin, J.; Qiao, B. T.; Li, N.; Li, L.; Sun, X. C.; Liu, J. Y.; Wang, X. D.; Zhang, T. Little do more: A highly effective Pt_1/FeO_x single-atom catalyst for the reduction of NO by H_2. *Chem. Commun.* **2015**, *51*, 7911–7914.

[93] Xu, G.; Wei, H. S.; Ren, Y. J.; Yin, J. Z.; Wang, A. Q.; Zhang, T. Chemoselective hydrogenation of 3-nitrostyrene over a Pt/FeO_x pseudo-single-atom-catalyst in CO_2-expanded liquids. *Green Chem.* **2016**, *18*, 1332–1338.

[94] Wei, H. S.; Liu, X. Y.; Wang, A. Q.; Zhang, L. L.; Qiao, B. T.; Yang, X. F.; Huang, Y. Q.; Miao, S.; Liu, J. Y.; Zhang, T. FeO_x-supported platinum single-atom and pseudo-single-atom catalysts for chemoselective hydrogenation of functionalized nitroarenes. *Nat. Commun.* **2014**, *5*, 5634.

[95] Tian, M. Z.; Liu, S. J.; Wang, L. L.; Ding, H.; Zhao, D.; Wang, Y. Q.; Cui, J. H.; Fu, J. F.; Shang, J.; Li, G. K. Complete degradation of gaseous methanol over Pt/FeO_x catalysts by normal temperature catalytic ozonation. *Environ. Sci. Technol.* **2020**, *54*, 1938–1945.

[96] Kresse, G.; Joubert, D. From ultrasoft pseudopotentials to the projector augmented-wave method. *Phys. Rev. B* **1999**, *59*, 1758–1775.

[97] Kresse, G.; Hafner, J. *Ab initio* molecular dynamics for liquid metals. *Phys. Rev. B* **1993**, *47*, 558–561.

[98] Perdew, J. P.; Burke, K.; Ernzerhof, M. Generalized gradient approximation made simple. *Phys. Rev. Lett.* **1996**, *77*, 3865–3868

[99] Blöchl, P. E. Projector augmented-wave method. *Phys. Rev. B* **1994**, *50*, 17953–17979.

[100] Dudarev, S. L.; Botton, G. A.; Savrasov, S. Y.; Szotek, Z.; Temmerman, W. M.; Sutton, A. P. Electronic structure and elastic properties of strongly correlated metal oxides from first principles: LSDA + U, SIC-LSDA and EELS study of UO_2 and NiO. *Phys. Status Sol.* **1998**, *166*, 429–443.

[101] Liechtenstein, A. I.; Anisimov, V. I.; Zaanen, J. Density-functional theory and strong interactions: Orbital ordering in Mott–Hubbard insulators. *Phys. Rev. B* **1995**, *52*, R5467–R5470.

[102] Delley, B. An all-electron numerical method for solving the local density functional for polyatomic molecules. *J. Chem. Phys.* **1990**, *92*, 508–517.

[103] Henkelman, G.; Jónsson, H. A dimer method for finding saddle points on high dimensional potential surfaces using only first derivatives. *J. Chem. Phys.* **1999**, *111*, 7010–7022.

[104] Henkelman, G.; Jónsson, H. Improved tangent estimate in the nudged elastic band method for finding minimum energy paths and saddle points. *J. Chem. Phys.* **2000**, *113*, 9978–9985.

[105] Henkelman, G.; Uberuaga, B. P.; Jónsson, H. A climbing image nudged elastic band method for finding saddle points and minimum energy paths. *J. Chem. Phys.* **2000**, *113*, 9901–9904.

[106] Medford, A. J.; Shi, C.; Hoffmann, M. J.; Lausche, A. C.; Fitzgibbon, S. R.; Bligaard, T.; Nørskov, J. K. CatMAP: A software package for descriptor-based microkinetic mapping of catalytic trends. *Catal. Lett.* **2015**, *145*, 794–807.

[107] Pyykkö, P.; Atsumi, M. Molecular single-bond covalent radii for elements 1–118. *Chem.—Eur. J.* **2008**, *15*, 186–197.

[108] Jiang, F.; Wang, S. S.; Liu, B.; Liu, J.; Wang, L.; Xiao, Y.; Xu, Y. B.; Liu, X. H. Insights into the influence of CeO_2 crystal facet on CO_2 hydrogenation to methanol over Pd/CeO_2 catalysts. *ACS Catal.* **2020**, *10*, 11493–11509.

[109] Tost, A.; Widmann, D.; Behm, R. J. Stable active oxygen on mesoporous Au/TiO_2 supported catalysts and its correlation with the CO oxidation activity. *J. Catal.* **2009**, *266*, 299–307.

[110] Yin, P.; Yu, J.; Wang, L.; Zhang, J.; Jie, Y.; Chen, L. F.; Zhao, X. J.; Feng, H. S.; Yang, Y. S.; Xu, M. et al. Water–gas-shift reaction on Au/TiO_{2-x} catalysts with various TiO_2 crystalline phases: A theoretical and experimental study. *J. Phys. Chem. C* **2021**, *125*, 20360–20372.

[111] Liu, X. Y.; Ma, Z. Y.; Gao, X. H.; Bai, M. M.; Ma, Y. J.; Meng, Y. Water gas shift reaction activity on Fe (110): A DFT study. *Catalysts* **2022**, *12*, 27.

[112] Wang, R. Y.; Guo, L. J.; Jin, H.; Lu, L. B.; Yi, L.; Zhang, D. M.; Chen, J. DFT study of the enhancement on hydrogen production by alkaline catalyzed water gas shift reaction in supercritical water. *Int. J. Hydrogen Energy* **2018**, *43*, 13879–13886.

[113] Zhu, M. H.; Wachs, I. E. Determining number of active sites and TOF for the high-temperature water gas shift reaction by iron oxide-based catalysts. *ACS Catal.* **2016**, *6*, 1764–1767.

[114] Keturakis, C. J.; Zhu, M. H.; Gibson, E. K.; Daturi, M.; Tao, F.; Frenkel, A. I.; Wachs, I. E. Dynamics of CrO_3–Fe_2O_3 catalysts during the high-temperature water–gas shift reaction: Molecular structures and reactivity. *ACS Catal.* **2016**, *6*, 4786–4798.

[115] Gunawardana, P. V. D. S.; Lee, H. C.; Kim, D. H. Performance of copper–ceria catalysts for water gas shift reaction in medium temperature range. *Int. J. Hydrogen Energy* **2009**, *34*, 1336–1341.

[116] Na, H. S.; Shim, J. O.; Ahn, S. Y.; Jang, W. J.; Jeon, K. W.; Kim, H. M.; Lee, Y. L.; Kim, K. J.; Roh, H. S. Effect of precipitation sequence on physicochemical properties of CeO_2 support for hydrogen production from low-temperature water–gas shift reaction. *Int. J. Hydrogen Energy* **2018**, *43*, 17718–17725.